

On the Emmenthal distribution of highly inclined asteroids

V. Carruba[★] and J. F. Machuca

UNESP, Univ. Estadual Paulista, Grupo de dinâmica Orbital e Planetologia, Guaratinguetá, SP, 12516-410, Brazil

Accepted 2011 August 1. Received 2011 July 11; in original form 2011 March 25

ABSTRACT

Highly inclined asteroids are objects with $\sin(i) > 0.3$. Among highly inclined asteroids, we can distinguish between objects with inclinations smaller than that of the centre of the $\nu_6 = g - g_6$ secular resonance and objects at higher inclinations. Using the current mechanisms of dynamical mobility, it is not easy to increase the values of an asteroid with an initial small inclination to values higher than that of the centre of the ν_6 resonance. The presence of highly inclined objects might therefore be related to the early phases of the Solar system.

It has been observed that several dynamically stable regions are characterized by a very low number density of objects, unlike low-inclined bodies that tend to occupy all the dynamically viable regions. The distribution of asteroids at a high inclination in the domain of proper elements in dynamically stable regions resembles an Emmenthal cheese, with regions of low number density close to highly populated areas. While this phenomenon has been observed qualitatively in the past, no quantitative study has yet been carried out on the extent and long-term stability of these regions.

In this paper, we identify two dynamically stable regions characterized by very low values of number density and permanence times of 100 Myr or more when the Yarkovsky force is considered. We show that the low number density of objects in these areas cannot be produced as a statistical fluctuation of any simple one-dimensional statistical distribution, such as the Poissonian, uniform and Gaussian distributions, or of a tri-dimensional distribution, such as the tri-variate normal distribution. The presence of unoccupied dynamically stable regions could indicate that the primordial asteroidal population might not have reached all available zones at high- i . This sets constraints on the scenarios for the early phases of the history of our Solar system.

Key words: celestial mechanics – minor planets, asteroids: general.

1 INTRODUCTION

Highly inclined asteroids are objects with $\sin(i) > 0.3$. For these bodies, the analytical theory used to obtain the proper elements is not very accurate. Highly inclined asteroids are also characterized by a non-uniform distribution. It has been observed that several dynamically stable regions are characterized by a very low number density of objects, unlike low-inclined bodies that tend to occupy all the dynamically viable regions. While this phenomenon has been observed qualitatively in the past (Carruba 2009b, 2010b; Michtchenko et al. 2010), no quantitative study has yet been carried out on the extent and long-term stability of these regions. This is important because it might provide information on the origin of the highly inclined population. If dynamically stable regions are not occupied, this could indicate that the primordial population might not have reached all available zones at high- i . This sets constraints

on the scenarios for the early phases of the history of our Solar system. The void zones in the asteroid distribution (in our analogy, the holes in the Emmenthal cheese), as well as the regions of higher asteroid number density, might therefore still carry the memory of events associated with the primordial phase of planetary migration.

In this paper, we investigate the long-term stability of underpopulated areas of highly inclined asteroids by using synthetic proper element maps and simulations of highly inclined real and fictitious objects, which include the Yarkovsky force. We then determine the probability that an originally uniform distribution of asteroids, a population following Poissonian or uni- and tri-variate Gaussian statistical distributions, describes the currently observed asteroid distribution.

This paper is arranged as follows. Having introduced the problem of stable underpopulated and overpopulated areas among highly inclined objects in the introduction, we revise the current knowledge on asteroid synthetic proper elements for highly inclined asteroids in Section 2. In Section 3, we discuss the orbital distribution of large asteroids and in Section 4 we consider statistically the probability

[★]E-mail: vcarruba@feg.unesp.br

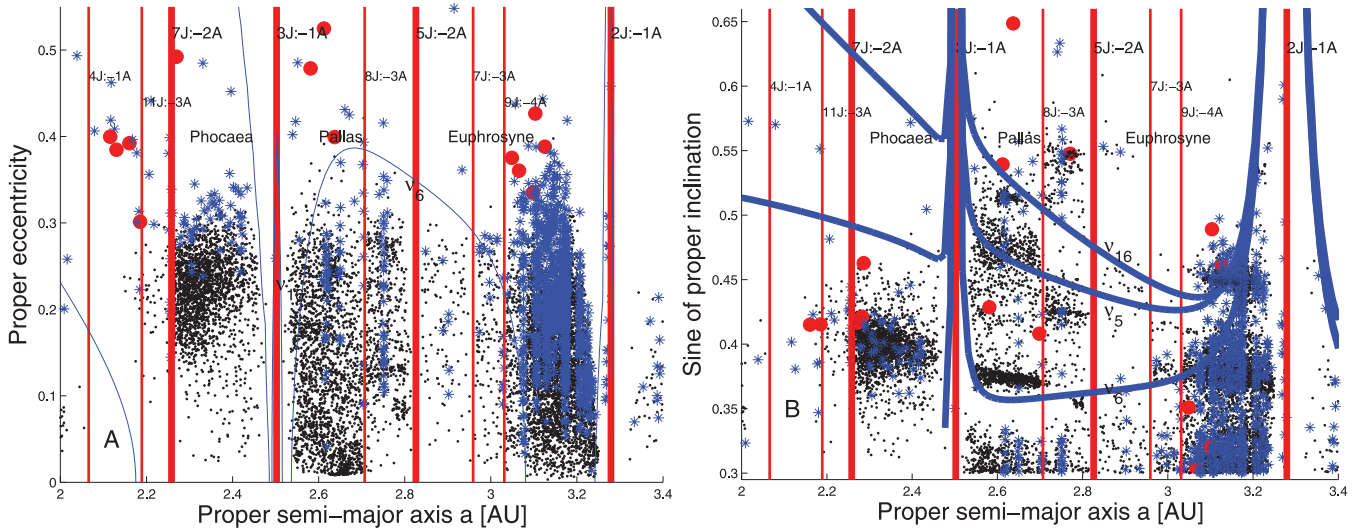


Figure 1. Panel A shows the (a, e) projection of highly inclined AstDyS asteroids. The blue asterisks display asteroids with a standard deviation on σ_a between 0.0003 and 0.01, while red circles show asteroids with σ_a larger than 0.01. The vertical red lines display the locations of mean-motion resonances, while the blue lines show the positions of linear secular resonances. Panel B shows the $[a, \sin(i)]$ projection of the same asteroids.

that various asteroid distributions might replicate the observed distribution. In Section 5, we obtain the number density distributions (density maps) of such objects for large ($H < 12$) and small objects, and we identify potential dynamically stable regions with a low number density of objects. In Section 6, we obtain synthetic proper-element maps for the underpopulated areas identified in Section 3. In Section 7, we study the long-term stability of these regions when the Yarkovsky force is considered. Finally, in Section 8, we present our conclusions.

2 SYNTHETIC PROPER ELEMENTS FOR HIGHLY INCLINED OBJECTS

The first step to identifying underpopulated dynamically stable regions is to have a reliable and updated set of asteroid proper elements. We start by revising the data available in the literature.

On 2010 December 8, the AstDyS site¹ listed a set of 240 831 asteroids for which the synthetic proper elements (and their errors) – obtained using the approach of Knežević & Milani (2003) – are available. We selected 10 073 objects of high inclination characterized by a semimajor axis in the range of 2.0–3.4 au and by $\sin(i) > 0.3$. We start by looking at projections in the (a, e) and $[a, \sin(i)]$ planes.

Fig. 1 displays (a, e) (panel A) and $[a, \sin(i)]$ (panel B) projections of the AstDyS proper elements for the highly inclined objects. Following Gil-Hutton (2006), we can divide the highly inclined population of asteroids into three regions: the Phocaea region (zone A in Gil-Hutton 2006) between the 7J:-2A and 3J:-1A mean-motion resonances, the Hansa and Pallas region (zone B) between the 3J:-1A and the 5J:-2A mean-motion resonances and the Euphrosyne region (zone C) between the 5J:-2A and the 2J:-1A mean-motion resonances. The thick vertical lines are associated with the main mean-motion resonances with Jupiter, while the thin lines show the location of higher-order mean-motion resonances. The blue lines show the location of the centre of the three main linear secular resonances ($\nu_6 = g - g_6$, $\nu_5 = g - g_5$ and $\nu_{16} = s - s_6$), computed using

the second-order and fourth-degree secular perturbation theory of Milani & Knežević (1992, 1994). Secular resonances occur when there is a commensurability between the precession frequency of an asteroid's pericentre g or node s and that of a planet g_i , s_i , where the suffix $i = 1, \dots, 8$ indicates the planet number as a function of the distance from the Sun (1 for Mercury, 2 for Venus, etc.). We warn the reader that the secular perturbation theory of Milani & Knežević (1992, 1994), which is based on an expansion in series of eccentricities and inclination of the perturbing function, loses accuracy at high inclination and close to mean-motion resonances. Thus, in Fig. 1 and in the subsequent figures, we report the location of the secular resonances given by this theory just as a qualitative indication, but we do not expect it to match the distribution of actual asteroids. The blue asterisks display asteroids with σ_a (the standard deviation of the values of the semimajor axis as computed with the approach of Knežević & Milani 2003) between 0.0003 au (the limit given by Knežević & Milani 2003 for ‘stable’ synthetic proper elements) and 0.01 au (the limit for pathological cases). The red circles show asteroids with σ_a larger than 0.01 au.² We remind the reader that objects at very high eccentricities (larger than about 0.4) are subject to close encounters with Mars and other planets, and are unstable on time-scales of a few Myr.

As can be seen in the figure, we can observe a region of low asteroid density near the ν_6 resonance border, which is caused by an increase in the eccentricity that asteroids on circulating and librating orbits experience because of the resonance topology (for a more in-depth discussion of the mechanism of asteroid depletion, see also Carruba 2010a; Carruba, Machuca & Gasparino 2011b). An exception to this mechanism is observed for asteroids in antialigned librating states of the ν_6 resonance, such as those of the Tina family (Carruba & Morbidelli 2011a), whose resonant states shield them from experiencing planetary close encounters. Besides the regions influenced by the ν_6 resonance, we can see a region of low asteroid

² Knežević & Milani define stable, unstable and pathological proper elements as elements having ‘small’, ‘medium’ and ‘large’ relative errors. The thresholds for the three cases with respect to each element are discussed in the text.

¹ Knežević & Milani (2003) <http://hamilton.dm.unipi.it/astdys>

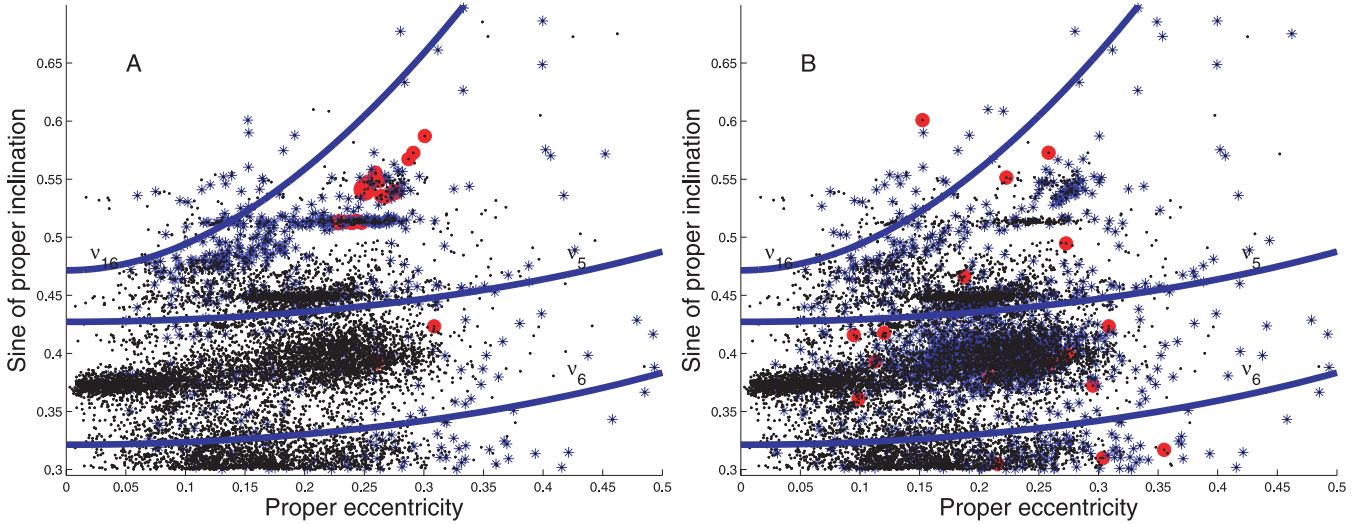


Figure 2. Panel A shows the $[e, \sin(i)]$ projection of highly inclined AstDyS asteroids. The blue asterisks display asteroids with a standard deviation on σ_e between 0.003 and 0.1, while the red circles show asteroids with σ_e larger than 0.1. The blue lines show the positions of linear secular resonances. Panel B shows the $[e, \sin(i)]$ projection of the same asteroids, but this time the blue asterisks display asteroids with a standard deviation on σ_i between 0.001 and 0.03, while the red circles show asteroids with σ_i larger than 0.03.

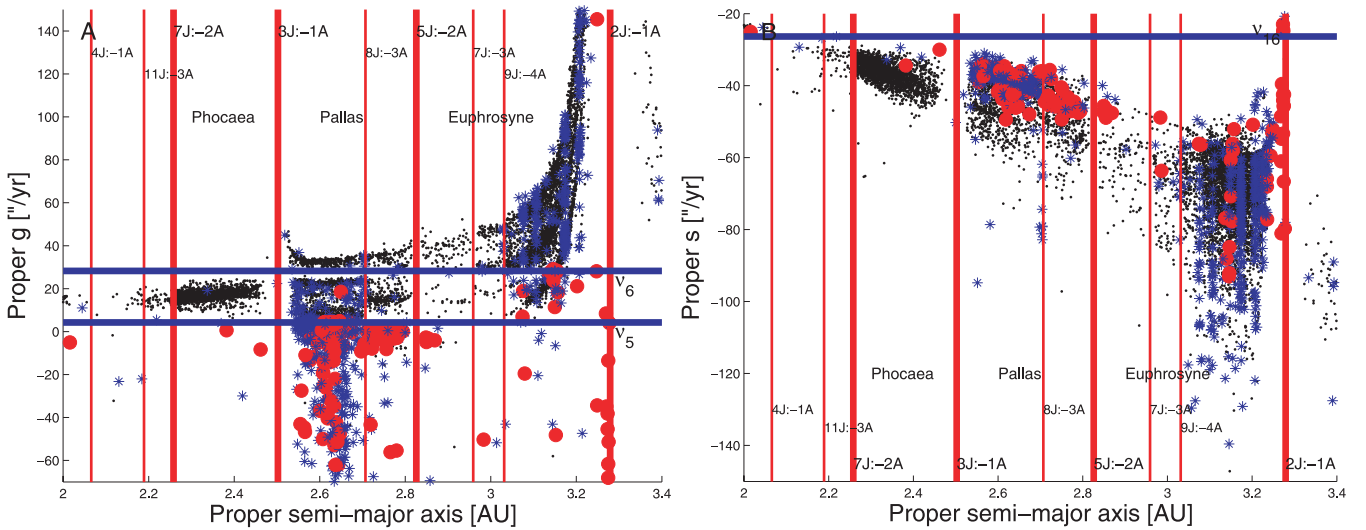


Figure 3. Panel A shows the (a, g) projection of highly inclined AstDyS asteroids. The blue asterisks display asteroids with a standard deviation on σ_g between 1 and 10, while the red circles show asteroids with σ_g larger than 10. Panel B shows the (a, s) projection of the same asteroids, but this time the symbols refer to σ_s (the range of values for the errors is the same).

density between the ν_5 and ν_{16} resonances in the $[a, \sin(i)]$ plane in the region of the Pallas family (see Fig. 1, panel B, and Carruba 2010b). More strikingly, there is a low-density region of asteroids between the 5J:-2A and 7J:-3A mean-motion resonances, which seems otherwise to be relatively stable. We investigate these subjects further in Sections 3 and 6.

In Fig. 2, we display $[e, \sin(i)]$ projections of asteroids with values of the errors in e (panel A) and i (panel B) for ‘stable’ (black dots), ‘unstable’ (blue circles) and ‘pathological’ (red circles) proper elements, according to Knežević & Milani (2003). As in Fig. 1, the blue lines display the locations of the main secular resonances in the region. As can be seen, the errors in eccentricity and inclination are larger for asteroids at high inclination, with very few objects having large errors at low eccentricities.

Finally, Fig. 3 displays (a, g) (panel A) and (a, s) (panel B) projections of highly inclined AstDyS asteroids. We can see the

departure from a linear dependence for g values as a function of a near the 2J:-1A and 3J:-1A mean-motion resonances, as discussed by Carruba & Michtchenko (2009). The negative values of g near the Hansa family are related to objects with small proper eccentricities ($e < 0.0179$), and to the problem of determining the correct proper frequency g for asteroids whose elements (k, h) pass through zero (Carruba 2010b). The ‘inclined’ dependence of s values as a function of a is discussed by Carruba & Michtchenko (2007).

3 ASTEROID ORBITAL DISTRIBUTION

When studying the current orbital distribution of objects, it is necessary to distinguish between ‘large’ and ‘small’ asteroids. Large objects have experienced very little orbital mobility, which is caused by the Yarkovsky effect, and it can be assumed that their current position is not far from the position they reached during the last stages

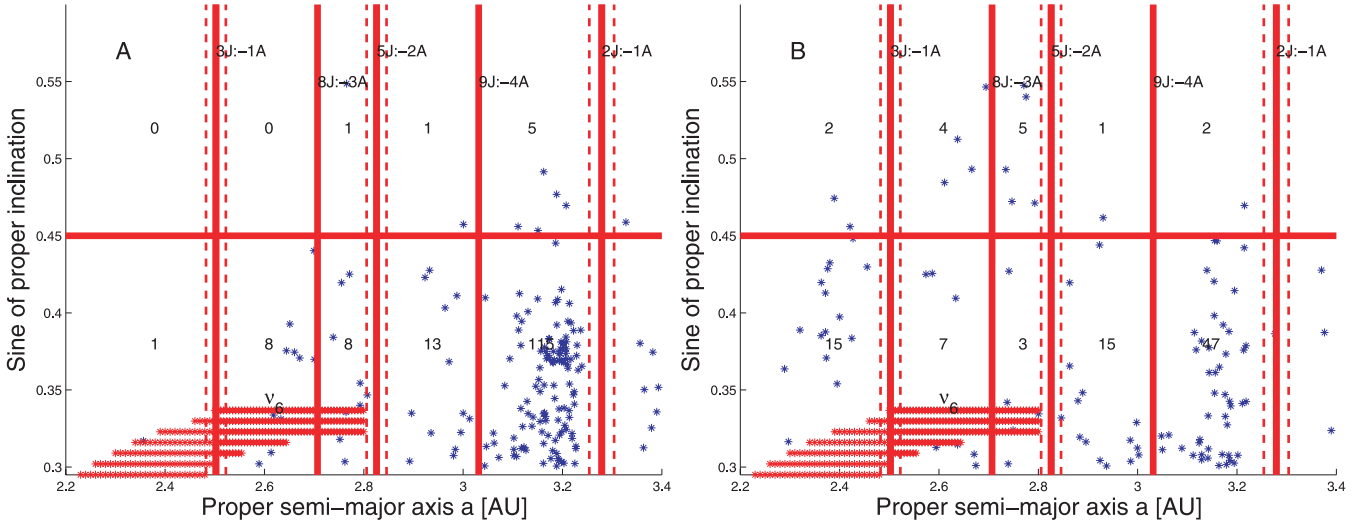


Figure 4. An $[a, \sin i(i)]$ plot of low-eccentricity ($e < 0.175$) $H < 12$ asteroids (panel A) and high-eccentricity ($e > 0.175$) $H < 12$ asteroids (panel B). The red asterisks identify regions affected by the ν_6 resonance, according to the model of Yoshikawa (1987). The dashed vertical lines display regions partially depopulated of asteroids near the mean-motion resonances.

of planetary migration. However, small objects tend to be displaced by the Yarkovsky force and, as a result, by mean-motion and secular resonances. Their current distribution can provide hints about the dynamical stability of the regions: underpopulated areas might be associated with dynamical unstable regions (but not necessarily, as we see later in this paper).

We define a ‘large’ object as an asteroid with an absolute magnitude $H > 12$. We choose this criterion because asteroids with this absolute magnitude are not significantly affected by non-gravitational effects. If we estimate the asteroid diameter using the relationship (Carruba et al. 2003)

$$D = \frac{D_0}{\sqrt{p_V}} \times 10^{-0.2H}, \quad (1)$$

where $D_0 = 1329$ km, p_V is the geometric albedo and H is the asteroid’s absolute magnitude. Even for very large values of $p_V = 0.5$, an asteroid with $H = 12$ will have a diameter of 7.5 km. At this size, the YORP effect is negligible. Using an obliquity of the spin axis of $\pm 90^\circ$ and parameters typical of C-type asteroids (Carruba et al. 2003), the mobility caused by the Yarkovsky force is at most 0.1635 au over 4.5 Gyr. Therefore, we should not expect the current orbital locations of such bodies to have changed much since the formation of the Solar system.³

To investigate the locations of stable areas characterized by a low population of objects, we have obtained the distribution of the number density of asteroids in the $[a, \sin(i)]$ representative plane. We concentrate on the $[a, \sin(i)]$ plane because we are interested in areas that were originally depleted in asteroids, and eccentricities are more easily changed by mechanisms of dynamical mobility than by proper inclinations (semimajor axes are affected by the Yarkovsky force). Regions in the $[a, \sin(i)]$ plane with inclinations different

from those of the bodies originally injected in highly inclined orbits can therefore still be characterized by a relatively low number density of objects.

To identify regions that were originally underpopulated, we need to eliminate areas whose low number density is caused by the destabilizing effects of the local dynamics. Based on several previous studies of the dynamics of highly inclined objects (see, for instance, Carruba 2009a,b, 2010a,b; Carruba et al. 2011b), we can distinguish between destabilizing resonances (resonances that cause a change in the asteroid eccentricity that is large enough to bring its pericentre to regions of terrestrial planet encounters, causing the loss of at least 50 per cent of the bodies initially inside the resonance because of a collision with the Sun or other planets during time-scales of 10 Myr or less, in conservative simulations of the orbital evolution of an asteroid subjected to the influence of the Sun and all the planets) and diffusive resonances (resonances whose passage through causes a significant change in the asteroid proper elements, but not large enough to cause the loss of the body). We can safely assume that bodies in regions affected by or near destabilizing resonances will be lost on time-scales of up to 10 Myr, so that local low densities do not reflect a non-uniform primordial distribution. The destabilizing effect of the resonances discussed are also investigated in some detail later in this paper.

Among destabilizing mean-motion resonances, we can identify from previous works the 7J:-2A, 3J:-1A, 5J:-2A and 2J:-1A mean-motion resonances with Jupiter. Fig. 4 shows $[a, \sin(i)]$ projections of asteroids with absolute magnitude $H < 12$ in the highly inclined area. Following the example of Michtchenko et al. (2010), we divided the population of objects into low-eccentricity ($e < 0.175$; Fig. 4, panel A) and high-eccentricity ($e > 0.175$; Fig. 4, panel B) asteroids. Both panels show vertical band (red dashed lines) that are related to the boundaries of the unstable regions associated with the destabilizing mean-motion resonances. To estimate the sizes of these boundaries, we used the following procedure. First, we computed the size of the resonance in the (a, e) plane using the approach described in Morbidelli (2002). Then, we added 0.015 au, the size of the depopulated region near the borders of the 3J:-1A mean-motion resonance, as observed by Guillens, Vieira Martins & Gomes (2002), to the value of the size in the semimajor axis

³ Of course, the orbital mobility of an object depends on several other parameters than the absolute magnitude, such as the spin axis obliquity, the thermal inertia, the thermal conductivity, the surface density, the bond albedo, etc. Thus, this criterion is approximated at best. However, because many of these parameters are not known for large numbers of asteroids, it is helpful to have a simple criterion that can be used for statistical considerations.

Table 1. Cell identification, the limits in a , e and $\sin(i)$, and the number of real $H < 12$ objects.

Cell identification	Intervals in a	Intervals in e	Intervals in $\sin(i)$	No. of real $H < 12$ objects
1	$a < a_{31}$	$e < 0.175$	$0.3 < \sin i < 0.45$	1
2	$a < a_{31}$	$e < 0.175$	$\sin i > 0.45$	0
3	$a < a_{31}$	$0.175 < e < 0.6$	$0.3 < \sin i < 0.45$	15
4	$a < a_{31}$	$0.175 < e < 0.6$	$\sin i > 0.45$	2
5	$a_{31} < a < a_{83}$	$e < 0.175$	$0.3 < \sin i < 0.45$	8
6	$a_{31} < a < a_{83}$	$e < 0.175$	$\sin i > 0.45$	0
7	$a_{31} < a < a_{83}$	$0.175 < e < 0.6$	$0.3 < \sin i < 0.45$	7
8	$a_{31} < a < a_{83}$	$0.175 < e < 0.6$	$\sin i > 0.45$	4
9	$a_{83} < a < a_{52}$	$e < 0.175$	$0.3 < \sin i < 0.45$	8
10	$a_{83} < a < a_{52}$	$e < 0.175$	$\sin i > 0.45$	1
11	$a_{83} < a < a_{52}$	$0.175 < e < 0.6$	$0.3 < \sin i < 0.45$	3
12	$a_{83} < a < a_{52}$	$0.175 < e < 0.6$	$\sin i > 0.45$	5
13	$a_{52} < a < a_{94}$	$e < 0.175$	$0.3 < \sin i < 0.45$	13
14	$a_{52} < a < a_{94}$	$e < 0.175$	$\sin i > 0.45$	1
15	$a_{52} < a < a_{94}$	$0.175 < e < 0.6$	$0.3 < \sin i < 0.45$	15
16	$a_{52} < a < a_{94}$	$0.175 < e < 0.6$	$\sin i > 0.45$	1
17	$a_{94} < a < a_{21}$	$e < 0.175$	$0.3 < \sin i < 0.45$	115
18	$a_{94} < a < a_{21}$	$e < 0.175$	$\sin i > 0.45$	5
19	$a_{94} < a < a_{21}$	$0.175 < e < 0.6$	$0.3 < \sin i < 0.45$	47
20	$a_{94} < a < a_{21}$	$0.175 < e < 0.6$	$\sin i > 0.45$	2

calculated at $e = 0.25$, the mean value of the eccentricity of asteroids in the region. Asteroids in these areas can be destabilized by mean-motion resonances either directly or indirectly via migration caused by the Yarkovsky force.

Concerning secular resonances, we considered the effect of the ν_6 resonance, and we computed the unstable regions using the criterion described in Carruba (2010a) and Carruba et al. (2011b). We first computed the k_6 parameter, defined as

$$k_6 = b - \nu_6, \quad (2)$$

where $\nu_6 = 28.243 \text{ arcsec yr}^{-1}$ is the precession frequency of Saturn's pericentre and b is a frequency-like parameter computed using the Yoshikawa (1987) model of the ν_6 resonance. Asteroids with k_6 values in the interval to $-2.55 < k_6 < 2.55 \text{ arcsec yr}^{-1}$ in the internal main belt (values of a smaller than the centre of the 3J:-1A mean-motion resonance; Carruba 2010a) and in the interval $-3.5400 < k_6 < 1.6815 \text{ arcsec yr}^{-1}$ in the central main belt (between the 3J:-1A and 5J:-2A mean-motion resonances; Carruba et al. 2011b) are considered likely to have their eccentricity pushed to terrestrial planet-crossing levels and to be destabilized on time-scales of 10 Myr.⁴ In the external main belt, it is not possible to use the Yoshikawa approach because of the perturbing effect of the 2J:-1A mean-motion resonance, not accounted for in the model. However, the effect of the ν_6 resonance is more limited in this region of the asteroid belt than in the internal part (see Section 6).

In order to have a sample of objects as close as possible to the primordial population, we have eliminated from the list of 313 highly inclined $H < 12$ asteroids those objects that are members of the following families: Phocaea, Barcelona, Hansa, Gersuind, Pallas, Gallia, Tina, Euphrosyne, Alauda, Luthera and (16708) (1995 SP1); see Carruba (2009b, 2010b) for the determination of the family membership of highly inclined objects. This left us with a list

⁴ The exception is the Tina family members in the central main belt whose orbits have k_6 values in the range discussed in Carruba et al. (2011b), but whose eccentricities do not reach planet-crossing levels because of the protecting effect of the antialigned ν_6 resonant configuration, as discussed in Carruba & Morbidelli (2011a).

of 253 asteroids whose current orbits should not have been greatly modified since the formation of the asteroid belt.

Then, we divided the highly inclined asteroid regions into 20 areas according to these criteria. We have used the main mean-motion resonances with Jupiter as ‘natural dynamical boundaries’ and we have created five regions: $a < a_{31}$, $a_{31} < a < a_{83}$, $a_{83} < a < a_{52}$, $a_{52} < a < a_{94}$ and $a_{94} < a < a_{21}$.⁵ This division creates slightly unequal cells in the semimajor axis, but we believe that this inconvenience is more than compensated by the fact that such a division respects the local dynamics and does not tend to incorporate in the same cell objects belonging to different dynamical groups. We then divided the asteroids into two large eccentricity cells, one for objects with $e < 0.175$ and the other for objects with larger eccentricity. We assume that, as observed, no asteroid has an eccentricity larger than 0.6, so that the limits of the cells at high eccentricity are $0.175 < e < 0.6$. Finally, we also created two cells in inclination separated by the value $\sin(i) = 0.45$, which roughly corresponds to the inclination of the centre of the ν_5 resonance in the central main belt. Overall, we created 20 cells in the $[a, e, \sin(i)]$ domain. Fig. 4 shows $[a, \sin(i)]$ projections of low-eccentricity ($e < 0.175$; panel A) and high eccentricity ($e > 0.175$; panel B) objects. Real asteroids in the region, selected according to the criterion described earlier in this section, are identified as blue asterisks, and the numbers in each cell are related to the number of objects per cell. Table 1 displays the cell numbers (from 1 to 20), the intervals in a , e and $\sin i$ of each cell and the number of real objects in each cell.

From this preliminary analysis, we can see that the number of $H < 12$ objects above the ν_6 resonance is indeed limited, especially at low eccentricities. We have identified 23 objects at low eccentricities ($e < 0.175$) and 59 objects at high eccentricities [$e > 0.175$; (2) Pallas is one of these objects]. These are characterized as having values of proper g , the frequency of precession of the pericentre, lower than $28.243 \text{ arcsec yr}^{-1}$, a value that corresponds to the ν_6 resonance. The limited number of large objects above the ν_6 resonance

⁵ For the cell boundaries, we have used the centre of the resonance, and the suffixes (e.g. 21) refer to the mean-motion resonances.

when compared with the analogous population at lower inclinations could suggest that the original population of highly inclined objects was limited to begin with.

4 STATISTICAL CONSIDERATIONS

In the previous sections, we have seen that there are large variations in the orbital distribution of asteroids in highly inclined regions. In this section, we try to understand whether this phenomenon is compatible with normal statistical fluctuations of a uniformly spaced or Gaussian-spaced population or whether we need some further hypothesis on the mechanisms that formed the original highly inclined populations. In our statistical analysis, we use two approaches. First, we consider the one-dimensional probability distributions for the $H < 12$ asteroid population using the cells defined in Section 3, checking for possible correlations among cells. Secondly, we try to see if the $[a, e, \sin(i)]$ tri-dimensional distribution follows a tri-variate Gaussian distribution by performing a normality test. We start by looking at the one-dimensional probability distributions.

4.1 One-dimensional probability distributions

When looking at one-dimensional probability distributions, there are two possible approaches. We can look at the $H < 12$ asteroid population and verify whether it follows simple one-dimensional probability distributions, such as the Poissonian, uniform or Gaussian distributions, in each cell. We can also check if there are correlations among cells at same inclinations or in the same range of semimajor axes. We start our analysis by looking at the Poissonian statistical distribution.

Table 2 displays the cell identification, as given in Table 1, the number of real objects in each cell, the weighted mean number of objects per cell, the probability that this number is generated by Poissonian statistics, the number of objects that would be produced in each cell if we assume a uniform distribution of objects in $[a,$

$e, \sin(i)]$, which best fit the data, and the number of objects that would be produced if we assume a Gaussian distribution in $[a, e, \sin(i)]$, which best fit the data. We have found that the $H < 12$ asteroid population has mean values of a, e and $\sin(i)$ of 3.0270 au, 0.1516 and 0.3656, respectively. The variances in a, e and $\sin(i)$ are 0.0653 au, 0.0057 and 0.0030, respectively. We have estimated the probability that a number of objects are produced by the Poissonian distribution, assuming that the expected number of k occurrences in a given interval is given by

$$f(k, \lambda) = \frac{\lambda^k e^{-\lambda}}{k!}. \quad (3)$$

Here, λ is a positive real number, equal to the expected number of occurrences in the given interval. For our purposes, we used for λ the mean values of objects per cell of real asteroids, weighted to account for the different volume occupied by each cell. This is given by

$$\lambda = N_{\text{ast}} \frac{V_{\text{cell}}}{V_{\text{Tot}}}, \quad (4)$$

where N_{ast} is the total number of objects with $H < 12$ in stable regions (253), V_{cell} is the volume in (a, e, i) space occupied by each cell – see Section 3 for the limits of the cell in the (a, e, i) domain – and V_{Tot} is the total volume in the region. Using standard statistical terminology, we define the null hypothesis as the possibility that the data are drawn from a given distribution. We can reject the null hypothesis if it is associated with a probability lower than a threshold that is usually of the order of 1 per cent or 0.01. Our results show that 13 cells have negligible probability that their numbers can be reproduced by a Poissonian distribution. The cells compatible with a Poissonian distribution (cells 5, 7, 8, 9, 11, 12 and 13) are those associated with the Hansa, Gallia and Brucato, Gersuind, Pallas and Danae regions. Other cells have an orbital distribution of highly inclined objects incompatible with a Poissonian distribution, either because they are underpopulated (cells 1, 2, 4, 6, 10, 14, 16, 18 and 20) or overpopulated (cells 3, 15, 17 and 19). Because 14 out of

Table 2. Number of real objects, the weighted mean number of objects per cell, the probability of real objects being a product of a Poissonian statistical distribution, the number of simulated objects with uniform and Gaussian distributions as a function of the cell in the $[a, e, \sin(i)]$ domain.

Cell identification	No. of real objects	Weighted mean number of objects per cell	Poissonian probability	Uniform distribution	Gaussian distribution
1	1	11.598	1.1×10^{-4}	15	2
2	0	18.761	7.1×10^{-9}	15	8
3	15	7.543	0.0058	41	51
4	2	18.320	1.8×10^{-6}	23	39
5	8	6.810	0.1264	4	1
6	0	16.548	6.5×10^{-8}	4	2
7	7	4.431	0.0792	18	31
8	4	10.760	0.0119	4	27
9	8	3.274	0.0123	7	2
10	1	7.950	0.0028	6	2
11	3	2.128	0.1913	8	11
12	5	5.170	0.1750	7	3
13	13	8.520	0.0400	6	5
14	1	20.692	2.1×10^{-8}	3	3
15	15	5.540	0.0004	19	10
16	1	13.457	1.9×10^{-5}	14	13
17	115	8.394	$< 10 \times 10^{-11}$	12	4
18	5	20.385	4.1×10^{-5}	6	3
19	47	5.459	$< 10 \times 10^{-11}$	20	14
20	2	13.257	1.5×10^{-4}	21	22

Overall, it seems that current non-uniformities in the number distributions of asteroids cannot be explained as fluctuations of one-dimensional statistical distributions, such as the Poissonian, uniform and Gaussian distributions, except possibly for the Phocaea region, which is marginally compatible with a Poissonian distribution of the inclinations. In the following subsection, we investigate if a multi-variate Gaussian distribution could better approximate our sample of large asteroids.

4.2 Tri-variate Gaussian probability distributions

In Section 4.1, we checked if one-dimensional probability distributions can account for the observed fluctuations in the number of large ($H < 12$) asteroids. Here, we investigate if a multidimensional distribution in the $[a, e, \sin(i)]$ domain, which accounts for possible correlations among the different dimensions, could better explain the observed distribution.⁷

We assume that the distribution in the $[a, e, \sin(i)]$ domain has a tri-variate Gaussian probability density function, given by

$$f(\mathbf{x}) = \frac{1}{(2\pi)^{3/2} \sqrt{|\Sigma|}} \exp \left[-\frac{1}{2} (\mathbf{x} - \boldsymbol{\mu})^T \Sigma^{-1} (\mathbf{x} - \boldsymbol{\mu}) \right]. \quad (6)$$

Here, \mathbf{x} is the vector $[a, e, \sin(i)]$ and $\boldsymbol{\mu}$ is the vector with components equal to the mean values of a , e and $\sin i$ of the observed population (see Section 4.1). Σ is the covariance matrix, which can be estimated numerically having n \mathbf{x}_j vectors using

$$\Sigma = \frac{1}{n} \sum_{j=1}^n (\mathbf{x}_j - \boldsymbol{\mu}) \cdot (\mathbf{x}_j - \boldsymbol{\mu})^T. \quad (7)$$

The numerical elements of Σ for the 253 highly inclined asteroids in the region are equal to

$$\Sigma = \begin{pmatrix} 0.0653 & -0.0066 & -0.0031 \\ -0.0066 & 0.0057 & 0.0007 \\ -0.0031 & 0.0007 & 0.0030 \end{pmatrix}. \quad (8)$$

$|\Sigma| = 9.2913 \times 10^{-7}$ au is the determinant of the covariance matrix. We first draw 253 random vectors from this tri-variate Gaussian distribution using the following procedure. Because Σ is positive defined, we use the Choleski decomposition to obtain a matrix \mathbf{A} such that $\mathbf{A} \cdot \mathbf{A}^T = \Sigma$. The \mathbf{A} matrix is a triangular matrix whose elements in the triangle below the main diagonal are all zero. We then generated 253 tri-dimensional vectors \mathbf{Z} , whose components are N independent standard normal variates, using standard MATLAB routines, such as `randn.m`, based on the Box–Muller transform. Finally, we obtained 1000 sets of 253 vectors in the $[a, e, \sin(i)]$ domain, following the given tri-variate Gaussian distribution, using

$$\mathbf{X} = \boldsymbol{\mu} + \mathbf{A}\mathbf{Z}. \quad (9)$$

These vectors have the desired distribution because of the affine transformation property; see Press et al. (2001) for information on the Choleski decomposition and see the MATLAB support website for information on `randn.m`. To check if the current observed asteroidal

population follows a tri-variate normal distribution, we performed two tests. First, we computed the number of generated fictitious asteroids per cell, using the cells defined in Section 3. Secondly, we performed a Pearson χ^2 test by computing a χ^2 -like variable defined by equation (5), where n_{int} is the number of intervals of our variables (20 in our case), q_i is the number of real objects in the i th interval and p_i is the number of simulated objects in the same interval. Once again, we remind the reader that values of χ^2 of the order of the number of intervals are consistent with a good fit. Even without considering the cells with $a_{94} < a < a_{21}$, whose large asteroidal population might be caused by the larger inclination values of the ν_6 resonance in the region (more asteroids could come to these areas from low-inclinations regions compared to other cells), we find that the lowest value of χ^2 for regions with $a < a_{94}$ is 73.22 for 16 intervals for a given set of the simulated 253 asteroids. Using the standard χ^2 probability distribution (Press et al. 2001), we find that the null hypothesis has a probability of just 5.3×10^{-10} , which is low enough for us to be able to reject it safely.

In order not to incur possible binning problems associated with our choice of cells, we also performed the Mardia test (Mardia 1970) on the multivariate normality for the whole 253 asteroid population.⁸ The Mardia test is based on multivariate extensions of skewness and kurtosis measures. For a sample (x_1, \dots, x_n) of p -dimensional vectors, we can compute the A and B parameters given by

$$A = \frac{1}{6n} \sum_{i=1}^n \sum_{j=1}^n [(\mathbf{x}_i - \boldsymbol{\mu})^T \Sigma^{-1} (\mathbf{x}_j - \boldsymbol{\mu})]^3 \quad (10)$$

and

$$B = \frac{\sqrt{n}}{\sqrt{8p(p+2)}} \times \left\{ \frac{1}{n} \sum_{i=1}^n [(\mathbf{x}_i - \boldsymbol{\mu})^T \Sigma^{-1} (\mathbf{x}_i - \boldsymbol{\mu})]^2 - p(p+2) \right\}. \quad (11)$$

Here, Σ^{-1} is the inverse of the covariance matrix given by equation (7). Under the null hypothesis of multivariate normality, the statistic A will have approximately a χ^2 distribution with $(1/6)p(p+1)(p+2)$ degrees of freedom (10 for $p=3$) and B will be approximately standard normal with a zero mean and a standard deviation equal to 1. We computed A and B for our sample of 253 asteroids and we obtained $A = 166.98$ and $B = 7156.20$, which have probabilities lower than 10^{-6} of being associated with χ^2 and normal distributions. Once again, we can safely assume that, on the whole, large highly inclined asteroids do not follow a tri-variate Gaussian distribution.

What about smaller samples of asteroids? To check this hypothesis, we again looked at asteroids in the same range of a , e and $\sin(i)$ as used in Section 4.1. We found that all asteroid samples have values of the Mardia test B parameter that are too high to satisfy the null hypothesis. However, the value of the A parameter for asteroids in the regions of Phocaea, Hansa and Pallas was below 10. This yielded a non-negligible probability (33 per cent for the lowest values of A of 7.7 in the Hansa region) that asteroids in the regions can be fitted by a tri-variate normal distribution. We also found a relatively small value of A for asteroids at very large inclinations ($A = 12.8$). While the large values of the B parameters should favour

⁷ We limit our analysis to the $[a, e, \sin(i)]$ proper-element domain because the g and, to a lesser extent, s frequencies are strongly perturbed in the proximity of mean-motion resonances, such as 2J:-1A and 3J:-1A (see Fig. 3). While there are techniques to normalize the dependence of the g frequency as a function of the mean-motion resonance or of the semimajor axis (Carruba & Michtchenko 2009), such a normalization requires an in-depth study of local family membership, which we feel is beyond the purposes of this study.

⁸ Other tests on multivariate normality, such as the tri-dimensional KS test (Fasano & Franceschini 1987), the Cox–Small test (Cox & Small 1978) and others, are also adequate choices for testing multivariate normality.

the exclusion of the null hypothesis, the fact that large asteroids in the same range of the semimajor axis are more likely to belong to tri-variate normal distributions could indicate that the mechanism that populated the highly inclined regions might have acted ‘vertically’ from lower values of inclinations to higher values, rather than ‘horizontally’, moving asteroids originally at the same inclinations to a different semimajor axis – with the possible exception of very highly inclined objects with $\sin(i) > 0.45$. Further studies on such a mechanism are needed before this hypothesis can be confirmed.

5 DENSITY MAPS

In Section 4, we analysed the statistical likelihood that fluctuations of the orbital distributions of asteroids at high inclination might be caused by fluctuations in the one- and three-dimensional statistical distributions. Here, we would like to address the dynamical causes of underpopulated and overpopulated areas by asking whether the observed underpopulated regions are caused by any dynamical mechanism.

Information on the dynamics of asteroids can be obtained by an analysis of the number densities of asteroids. Fig. 5 displays contour plots of such densities. See Carruba (2009b) for a description of the procedure used to generate such plots; here, we have used 70 steps of 0.02 au in a and 30 steps of 0.04 in $\sin(i)$. Higher number densities of objects are shown in whiter tones. Once again, we divided the population of objects into small-eccentricity bodies ($e < 0.175$; Fig. 5, panel A) and large-eccentricity bodies ($e > 0.175$; Fig. 5, panel B).

As can be seen in Fig. 5 (panels A and B), underpopulated areas (in black) in the Phocaea region are clearly associated with the border of the ν_6 secular resonance. Therefore, they can be understood within the framework of the interaction of the ν_6 resonance topology, which causes the asteroid eccentricity to increase, and of planetary close encounters, which remove such particles in short time-scales (see Carruba 2010a for an in-depth description of these mechanisms). In the Pallas area, we can identify an underpopulated area, especially visible at high eccentricities, between the 8J:-3A and 5J:-2A mean-motion resonances and the ν_5 and ν_{16} secular resonances (roughly, this corresponds to values of $\sin i$ between 0.45 and

0.50). This area is shown by white boxes in Fig. 5, and corresponds to cell 10 in Section 4, which has a low probability that the large asteroidal population follows a Poissonian distribution. The underpopulated area in the region between 2.5 and 2.82 au in a and 0.36 and 0.42 in $\sin(i)$ is caused by the presence of the ν_6 resonance. The destabilizing effect of this resonance on local asteroids has been studied in Carruba et al. (2011b) and in Carruba & Morbidelli (2011a). Finally, in the Euphrosyne area, the whole region above the ν_6 resonance and between the 5J:-2A and 9J:-4A mean-motion resonances is characterized by a remarkable low number density of objects. We have identified the underpopulated stable areas in Fig. 5 (panels A and B), corresponding to cells 14, 15 and 16 in Section 4, with white boxes. For comparison purposes, we also selected a region in a high asteroid population area in the Euphrosyne region. This region is identified by a green box in Fig. 5, and corresponds to the last four cells (17, 18, 19 and 20) in Section 4.

To investigate if these regions are dynamically stable or not, we performed a numerical analysis, the results of which are discussed in Section 6.

6 DYNAMICAL MAPS

We start by investigating the region between the 8J:-3A and 5J:-2A mean-motion resonances, previously identified in Section 3 as a stable region with a low asteroid population. For this purpose, we obtained the synthetic proper elements of 2160 test particles integrated with *swift_mvsv*, the integrator from the *swift* package (Levison & Duncan 1994) modified by Brož (1999), so as to include on-line digital filtering in order to remove all frequencies with periods less than 600 yr. We integrated the objects over 10 Myr. The synthetic proper elements were obtained with the procedure described in Knežević & Milani (2003), except for the proper frequencies, which were derived with the frequency modified Fourier transform (FMFT) of Šidlichovský & Nesvorný (1997) using the following procedure. We eliminated from the spectra of the Fourier transform of the equinoctial elements all planetary frequencies and we then assigned as the proper frequency the largest value in the spectra that was still observable, rather than fitting the time series of ϖ_f and Ω_f of the oscillations in the (k, h) and (p, q) planes. The test particles were integrated under the influence of all planets from

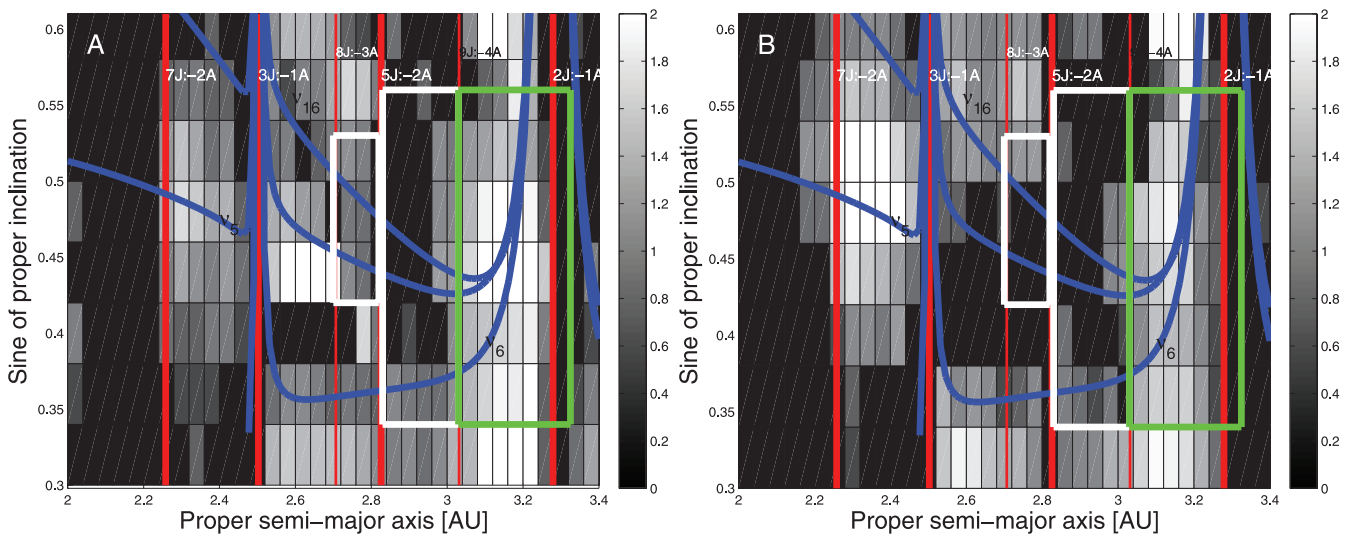


Figure 5. An $[a, \sin(i)]$ density map of low-eccentricity ($e < 0.175$, panel A) and high-eccentricity ($e > 0.175$, panel B) asteroids. The white boxes identify the underpopulated stable areas and the green box displays the stable sample area. The other lines have the same meanings as in Fig. 1.

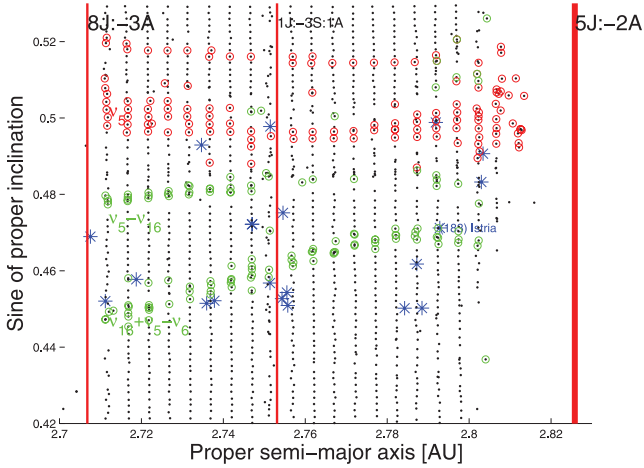


Figure 6. Synthetic proper-element map of the region of (183) Istria. The vertical lines display the mean-motion resonances, the blue asterisks identify real objects in the region, the red circles are associated with asteroids in linear secular resonances and the green circles display bodies in non-linear secular resonances.

Venus to Neptune (Mercury was accounted for as a barycentric correction of the initial conditions) and we referred the inclination and the arguments of pericentre and node to the invariable plane of the Solar system. The initial conditions of planets and particles were computed on 2000 January 1. Our test particles covered the interval between 2.7 and 2.83 au, and between 23° and 31° , and we set the values of initial eccentricity and other angles equal to those of (183) Istria, the real object in the area with the lowest identification. Finally, we used 27 intervals in a and 80 in i .

Fig. 6 shows the $[a, \sin(i)]$ projection of the synthetic proper elements of our test particles (black dots). Regions unaffected by resonances appear as regular vertical alignments of objects in this map, while areas affected by mean-motion resonances appear as void of asteroids (see the area near the 5J:-2A resonance). Objects in secular resonances appear to form inclined alignments. Vertical red lines show the locations of the main mean-motion resonances in the region, as identified in Carruba (2010b). Red circles show the objects to within $0.3 \text{ arcsec yr}^{-1}$ from the centre of the linear secular resonance in the region, $\nu_5 = g - g_5$. Green circles show the locations of the non-linear secular resonances in the area, $\nu_5 - \nu_{16} = g - g_5 - (s - s_6)$ and $\nu_{16} + \nu_5 - \nu_6 = s - s_6 + (g - g_5) - (g - g_6)$. For simplicity, we do not show secular resonances involving the Uranus frequency g_7 , such as the ν_7 resonance, because these are close in proper-element space to the resonances involving the g_5 frequency. Finally, real asteroids are identified by blue asterisks.

As can be seen, the region below the ν_5 resonance appears to be stable over the length of the integration (the role of non-linear secular resonances is investigated in Section 7, yet the number of real objects observed is very limited. Between $\sin(i)$ equal to 0.45 and 0.50, we only observe 21 objects, three of them with an absolute magnitude lower than 12.

To check if our results are independent of the choice of initial conditions and of the length of the integration, we also performed two numerical experiments. We integrated 1530 particles in the region with different initial conditions (the orbital elements of the planets and test particles were computed on 2010 January 1) and with the same initial conditions previously used, but for a longer time-scale. We find no significant difference concerning lost and unstable objects between the three simulations; however, there are

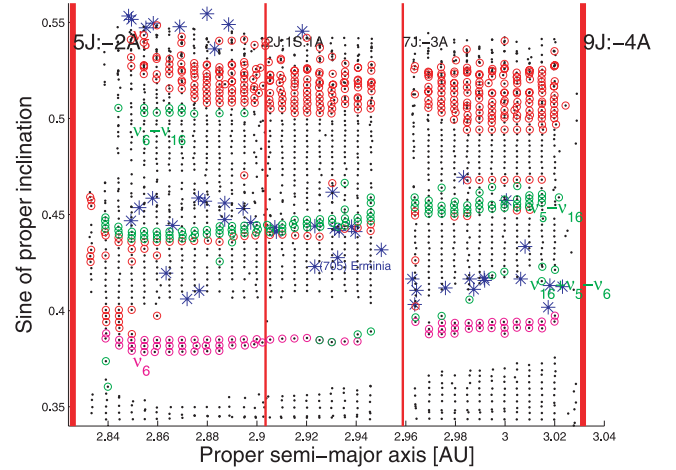


Figure 7. Synthetic proper-element map of the region of (705) Erminia. The magenta circles are associated with bodies in the ν_6 secular resonance. The other symbols are the same as in Fig. 6.

small differences concerning ≈ 30 particles in secular resonances, which have slightly different values of proper frequencies g and, in some cases, of proper $\sin(i)$. Because our goal is to study the long-term stability of test particles and not to focus on the details of secular dynamics, we believe that our choice of initial conditions and integration length should be reasonable.

We now turn our attention to the underpopulated area in the Euphrosyne region. To investigate the dynamical stability of this region, we integrated 3000 particles between 2.83 and 3.03 au (roughly speaking, between the 5J:-2A and 9J:-4A mean-motion resonances) and between 20° and 35° in inclination (corresponding to values of $\sin(i)$ between 0.20 and 0.55), under the same conditions as the previous simulation. The initial eccentricities and the other angles of the test particles were those of (705) Erminia, the lowest numbered object in the region.

Fig. 7 shows the synthetic proper-element map for this region. We can see the line of asteroids in ν_6 antialigned librating states (in magenta) that are stable near the centre of the unstable region as a result of the ν_6 resonance (see Carruba & Morbidelli 2011a for a description of the dynamics of asteroids in ν_6 antialigned librating states). As observed for the region around (183) Istria, the region between the ν_5 resonance (asteroids in this resonance are shown as red circles) and the ν_6 resonance appears to be stable, yet underpopulated. For this region, we observe the possible role that the $\nu_5 - \nu_{16}$, $\nu_6 - \nu_{16}$ and $\nu_{16} + \nu_5 - \nu_6$ non-linear secular resonances might play in the dynamical evolution of asteroids in the region. The long-term effect of these resonances when non-gravitational forces are present is discussed in Section 7.

Finally, we turn our attention to the highly populated area (the ‘test area’) in the Euphrosyne region discussed in Section 3. Using the same set-up as for the previous runs, we integrated 4500 particles between 3.03 and 3.325 au, and between 20° and 35° . The initial eccentricities and the other angles of the test particles were those of (31) Euphrosyne. Fig. 8 shows the synthetic proper-element map for this region. Particles in the ν_6 resonance are shown as magenta circles, those in ν_5 are identified by red circles⁹ and particles in the

⁹ The large number of red circles near the 2J:-1A mean-motion resonance is an effect of the perturbation caused by the resonance on the asteroid frequency g . This does not necessarily indicate that the particles are in a secular resonance.

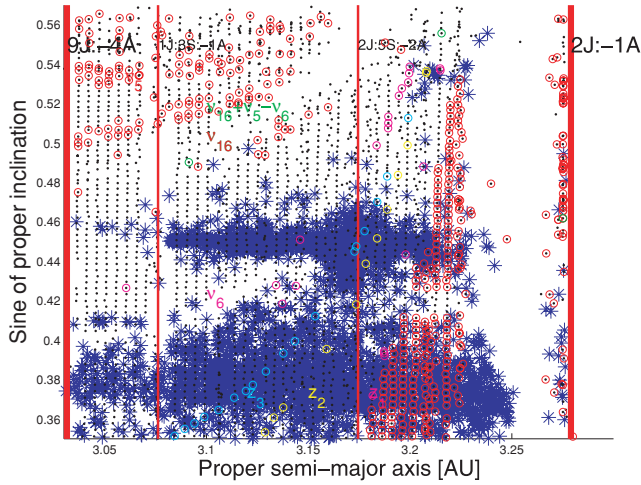


Figure 8. Synthetic proper-element map of the region of (31) Euphrosyne. The magenta circles show bodies inside the z_1 resonance, the yellow circles show asteroids inside the z_2 resonance and the cyan circles are associated with objects inside the z_3 resonance. The other symbols are the same as in Fig. 6.

ν_{16} resonance are indicated as green circles. The two main unstable areas in the Euphrosyne regions caused by secular resonances are associated with the ν_6 and ν_{16} resonances. We also show particles to within $0.3 \text{ arcsec yr}^{-1}$ of the $z_1 = \nu_6 + \nu_{16}$ resonance (magenta circles), of the $z_2 = 2\nu_6 + \nu_{16}$ resonance (yellow circles), of the $z_3 = 3\nu_6 + \nu_{16}$ resonance (cyan circles) and of the $\nu_{16} + \nu_5 - \nu_6$ resonance (green circles). Other secular resonances that are known to affect the orbits of real asteroids are the $\nu_5 + \nu_6$ and $2\nu_5 + \nu_6$ resonances (not shown for simplicity). We also observe the effects of the 1J:3S:-1A and 2J:5S:-2A three-body mean-motion resonances. Finally, real asteroids are identified by blue asterisks.

Two things can be noticed about the test area. First, the region is significantly affected by the presence of the 2J:-1A mean-motion resonance, which, with the exception of the population of asteroids near the resonance centre (the stable Zhongguos and the unstable Griquas populations; Roig, Nesvorný & Ferraz-Mello 2002), significantly destabilized objects near the resonance separatrix. Overall, the region is less ‘stable’ than the two regions previously studied,

yet it hosts a much larger asteroid population than that found in previous areas. Secondly, many of the objects found in the region are at an inclination lower than that of the ν_6 resonance centre. This leads us to wonder if the vast majority of the $\sin(i) > 0.3$ population in the Euphrosyne region might actually be considered as ‘highly’ inclined. In Section 7, we investigate further the long-term effect of the local web of resonances when non-gravitational forces are considered.

7 LONG-TERM STABILITY

To investigate the orbital evolution over a long time-span of particles in the areas discussed in the previous sections, we numerically integrated test particles with SWIFT-RMVSy, the symplectic integrator of Brož (1999), which simulates the diurnal and seasonal versions of the Yarkovsky effect. Because objects in the hole in the Pallas region are mostly of S-type (Carruba 2010b), we used values of the Yarkovsky parameters appropriate for such bodies (Carruba et al. 2003): a thermal conductivity $K = 0.001 \text{ W m}^{-1} \text{ K}^{-1}$, a thermal capacity $C = 680 \text{ J kg}^{-1} \text{ K}^{-1}$, a surface density 1500 kg m^{-2} , a Bond albedo of 0.1, a thermal emissivity of 0.95 and a bulk density of 2500 kg m^{-3} . We used two sets of spin-axis orientations, one with an obliquity of $+90^\circ$ and one with -90° with respect to the orbital plane, and periods obtained by assuming that the rotation frequency is inversely proportional to the object’s radius, and that a 1-km asteroid had a rotation period of 5 h (Farinella, Vokrouhlický & Hartmann 1998). We used particles with a radius of 2 km, and no reorientations were considered, so that the drift caused by the Yarkovsky effect was the maximum possible. We integrated the 2160 test particles of the first simulation over 100 Myr, the time-scale used to study the effect of proximity to the 3J:-1A mean-motion resonance by Guillens et al. (2002), under the gravitational influence of seven planets (Mercury was accounted for as a barycentric correction of the initial conditions).

Fig. 9 shows the maximum permanence times for our particles that remained in the hole 1 region as a function of the synthetic proper elements computed in Section 6. The black dots show objects with permanence times of less than 10 Myr while the red full circles are associated with particles with permanence times longer than 100 Myr. Blue asterisks show the orbital location of real asteroids

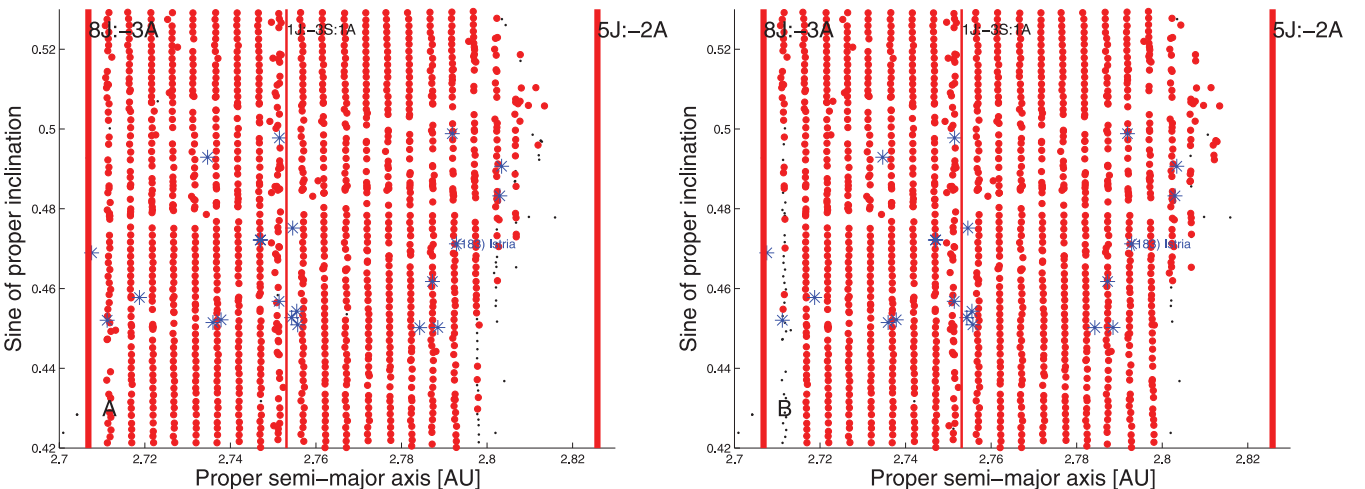


Figure 9. Maximum permanence times for particles in the hole 1 region for asteroids with an initial obliquity of $+90^\circ$ (panel A) and -90° (panel B). The black dots show objects with permanence times less than 10 Myr, while the red full circles are associated with particles with permanence times longer than 100 Myr. The other symbols are the same as in Fig. 1.

in the region. Panel A is associated with asteroids with an initial obliquity of $+90^\circ$ and panel B shows the fate of objects with initial obliquities of -90° . We note that most of the km-sized asteroid were not lost during the integration. Objects lost at times between 10 and 100 Myr were mostly particles close to the boundaries of the 5J:-2A and 8J:-3A mean-motion resonances. Overall, the region between the 5J:-2A and 8J:-3A mean-motion resonances seems to be quite stable for km-sized objects on a 100-Myr time-scale.

We then integrated the same 3000 test particles used for the dynamical map of the hole in the Euphrosyne region (see Section 6) over 100 Myr with *SWIFT-RMVS*. The set-up of the simulation was the same used for the particles in the Pallas hole, but here we used parameters for the Yarkovsky force typical of C-type asteroids, which are predominant in the Euphrosyne region (the same parameters as for an S-type asteroid, but with a bulk density of 1500 kg m^{-3} ; Carruba et al. 2003). See Gil-Hutton (2006) for a discussion of the spectral types of asteroids in the Euphrosyne region.

Fig. 10 shows the maximum permanence times for our particles that remained in the hole 2 region as a function of the synthetic proper elements computed in Section 6. The symbols used are the

same as for Fig. 9. Just as for the simulation for the Pallas hole, we observe that the layer of particles with permanence times of less than 10 Myr is limited to the boundaries of the main resonances in the region (5J:-2A, 7J:-3A, 9J:-4A and ν_6), but we observe that the rest of the region is stable for km-sized objects on a 100-Myr time-scale.

Finally, we turn our attention to the test area defined in Section 3. Fig. 11 shows maximum permanence times for the same 4500 particles in the area as a function of the synthetic proper elements computed in Section 6, assuming Yarkovsky parameters typical of C-type asteroids. The symbols used are the same as for Fig. 9. We observe that the region is overall stable over a 100-Myr time-scale, with the exceptions of asteroids in the 2J:-1A central island of stability and a few objects near the borders of the ν_6 , ν_{16} and 1J:3S:-1A resonances.

Because our dynamical analysis has shown that the studied underpopulated areas are dynamically stable, even when non-gravitational effects are considered, we have to conclude that the low population of objects in these regions is real, and is not caused by fluctuations in statistical distributions, as seen in Section 4. The

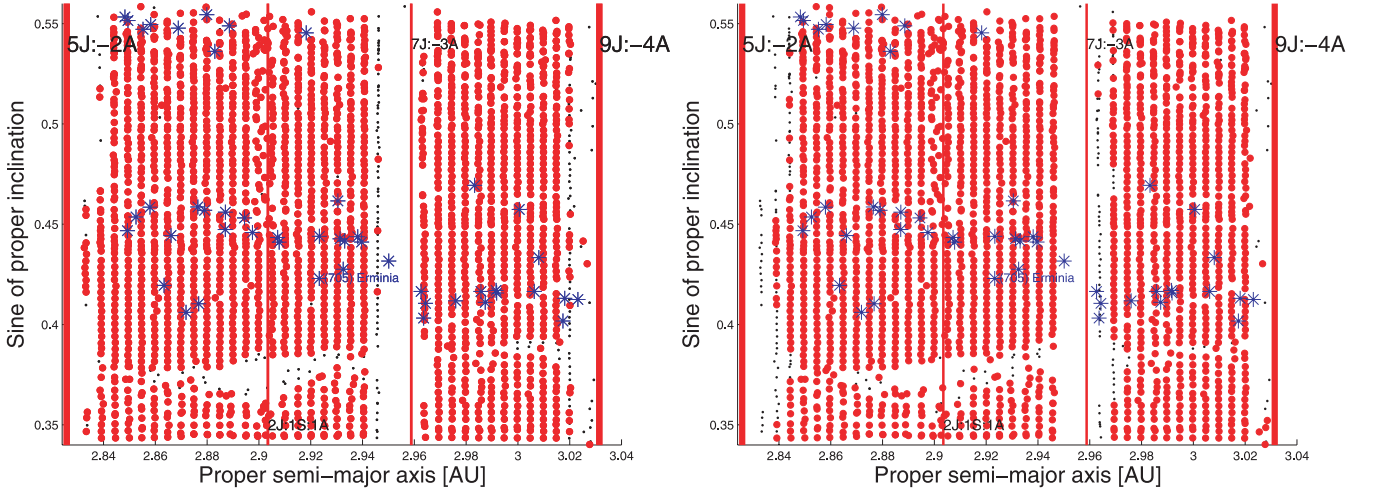


Figure 10. Maximum permanence times for particles in the hole 2 region for asteroids with an initial obliquity of $+90^\circ$ (panel A) and -90° (panel B). All symbols are the same as in Fig. 9.

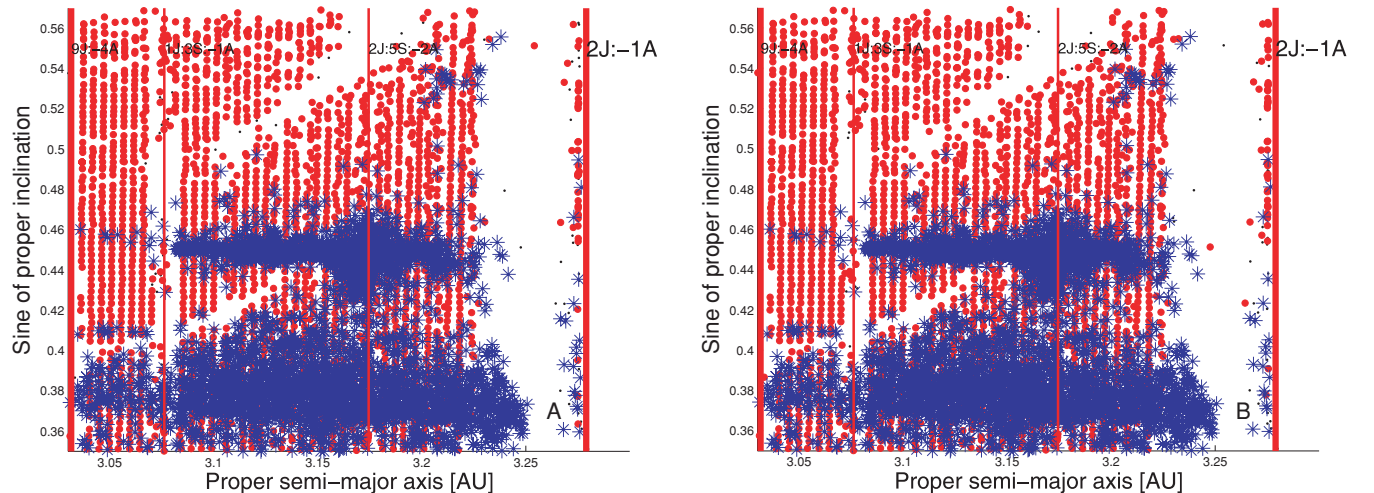


Figure 11. Maximum permanence times for particles in the test region for asteroids with an initial obliquity of $+90^\circ$ (panel A) and -90° (panel B). All symbols are the same as in Fig. 9.

low number of objects observed in these areas might therefore be a fossil indication of phenomena that occurred in the early phase of the formation of the Solar system.

8 CONCLUSIONS

(i) We have revised the knowledge of the synthetic proper elements of asteroids in the highly inclined region $\sin(i) > 0.3$. We have found 10 073 numbered objects from the AstDyS site between 2.0 and 3.4 au.

(ii) We have obtained synthetic proper-element maps for the two candidate regions and a test region with a high number density of asteroids. We have identified all the main two-, three- and four-body mean-motion and non-linear secular resonances in these areas.

(iii) We have verified the possibilities that dynamically stable regions can be explained as fluctuations of simple statistical one-dimensional distributions, such as Poissonian, uniform and Gaussian distributions. Our results show that, while asteroids in the Phocaea region might possibly follow a Poissonian distribution in inclinations, dynamically stable underpopulated regions cannot be explained as simple fluctuations of these statistical distributions. These must be caused either by disuniformities in the mechanism that populated the highly inclined regions or by some mechanism that depopulated the currently stable areas.

(iv) We verified the possibility that highly inclined asteroids might follow a tri-variate Gaussian probability distribution. Once again, we found that this is not likely. Multidimensional normality tests show that it is highly unlikely that highly inclined asteroids, as a whole, might follow a tri-variate normal distribution. Asteroids in the same range of semimajor axis in the Phocaea, Hansa and Pallas regions show a small but non-negligible probability of belonging to a tri-variate normal distribution. This could indicate that the mechanisms that populated the highly inclined regions might have acted ‘vertically’ from lower values of inclinations to higher, rather than ‘horizontally’ (i.e. moving asteroids originally at the same inclinations to different semimajor axes). The possible exception is very highly inclined objects with $\sin(i) > 0.45$. Further studies on such mechanisms are needed before this hypothesis can be confirmed.

(v) We have obtained density maps of the region and identified two areas that are characterized by low probabilities that the observed distributions of large asteroids might follow a Poissonian statistics. The first candidate area is in the central main belt (the Pallas region), while the second is in the outer main belt (the Euphrosyne region).

(vi) We have simulated the long-term dynamical evolution of test particles in these regions when the Yarkovsky force is considered. Despite the low number density of objects observed, the two areas with low number density were both mostly characterized by large permanence times, of the order of 100 Myr or more. These showed no significant qualitative differences from the highly populated test area.

Overall, our results show that the low number densities of asteroids in dynamically stable areas cannot be explained by simple fluctuations of Poissonian, uniform or Gaussian distributions. Some other mechanism has to be responsible for the observed non-uniformities. There are two hypotheses: (i) the current high-inclination population was created by a non-uniform mechanism; (ii) some as yet unknown dynamical effect depopulated the currently dynamically stable regions.

The first hypothesis could be coherent with what was observed by Ribeiro & Roig (2010) for the external main belt, where most of background objects seem to be associated with a family, suggesting that primordial bodies in the main belt are limited and scattered. The second hypothesis could justify the paucity of objects observed between the 5J:-2A and 9J:-4A mean-motion resonances, also noticeable in the main belt with a low inclination ($\sin(i) < 0.3$). However, there could be some difficulty explaining why the region of low asteroid density in the Pallas area is adjacent to a region of relatively high asteroidal populations at higher and lower inclinations. In any case, much more work is needed in order to understand the causes of the current ‘Emmenthal structure’ of the highly inclined asteroids.

ACKNOWLEDGMENTS

We thank the referee, Hagai Perets, for hints and suggestions that significantly improved the quality of this work. We are grateful to A. Morbidelli for discussions in which this work was conceived. We would like to thank the São Paulo State Science Foundation (FAPESP), which supported this work via the grant 06/50005-5, and the Brazilian National Research Council (CNPq, grants 302183/2008-6 and 473345/2009-9). We are also grateful to the Department of Mathematics of FEG-UNESP for allowing us to use their facilities.

REFERENCES

- Brož M., 1999, Thesis, Charles Univ., Prague, Czech Republic
- Carruba V., 2009a, MNRAS, 395, 358
- Carruba V., 2009b, MNRAS, 398, 1512
- Carruba V., 2010a, MNRAS, 403, 1834
- Carruba V., 2010b, MNRAS, 408, 580
- Carruba V., Michtchenko T., 2007, A&A, 475, 1145
- Carruba V., Michtchenko T., 2009, A&A, 493, 267
- Carruba V., Morbidelli A., 2011, MNRAS, 412, 2040
- Carruba V., Burns J. A., Bottke W., Nesvorný D., 2003, Icarus, 162, 308
- Carruba V., Machuca F., Gasparino H., 2011, MNRAS, 412, 2052
- Cox D. R., Small N. J. H., 1978, Biometrika, 65, 263
- Farinella P., Vokrouhlický D., Hartmann W. K., 1998, Icarus, 132, 378
- Fasano G., Franceschini A., 1987, MNRAS, 225, 155
- Gil-Hutton R., 2006, Icarus, 183, 93
- Guillens S. A., Vieira Martins R., Gomes R. S., 2002, AJ, 124, 2322
- Knežević Z., Milani A., 2003, A&A, 403, 1165
- Levison H. F., Duncan M. J., 1994, Icarus, 108, 18
- Mardia K. V., 1970, Biometrika, 57, 519
- Michtchenko T. A., Lazzaro D., Carvano J. M., Ferraz-Mello S., 2010, MNRAS, 401, 2499
- Milani A., Knežević Z., 1992, Icarus, 98, 211
- Milani A., Knežević Z., 1994, Icarus, 107, 219
- Morbidelli A., 2002, Modern Celestial Mechanics. Taylor and Francis, London
- Press V. H., Teukolsky S. A., Vetterlink W. T., Flannery B. P., 2001, Numerical Recipes in Fortran 77. Cambridge Univ. Press, Cambridge
- Ribeiro A. O., Roig F., 2010, in Fernandez J. A., Lazzaro D., Prialnik D., Schulz R., eds, Proc. IAU Symp. 263, Icy Bodies of the Solar System. Kluwer, Dordrecht, p. 237
- Roig F., Nesvorný D., Ferraz-Mello S., 2002, MNRAS, 335, 417
- Šidlichovský M., Nesvorný D., 1997, Celest. Mech. Dyn. Astron., 65, 137
- Yoshikawa M., 1987, Celest. Mech., 40, 233

This paper has been typeset from a \LaTeX file prepared by the author.